Investigation of alkali-ion (Li, Na, and K) intercalation in K_xVPO_4F cathode

*Haegyeom Kim, Yuji Ishado, Yaosen Tian, and Gerbrand Ceder**

Dr. H. Kim and Prof. G. Ceder
Materials Sciences Division, Lawrence Berkeley National Laboratory, Berkeley, CA 94720, USA
E-mail: gceder@berkeley.edu

Y. Ishado
Interdisciplinary Graduate School of Engineering Sciences, Kyushu University, Kasuga, Fukuoka 816-8580, Japan Country

Prof. G. Ceder and Y. Tian
Department of Materials Science and Engineering, University of California, Berkeley, CA 94720, USA

Keywords: Potassium, Sodium, Lithium, Batteries, Cathodes

Abstarct

This work compares the intercalation of K, Na, and Li in K_xVPO_4F (x~0). The K_xVPO_4F (x~0) cathode delivers reversible capacities of ~90–100 mAh g^{-1} in K, Na, and Li cells, at an average voltage of ~4.33 V for K, ~3.98 V for Na, and ~3.96 V for Li. This is so far the highest average voltage known for a K-intercalation cathode. The lower voltage of Li insertion compared to Na is attributable to undercoordinated Li ions in the K_xVPO_4F (x~0) framework. While the material shows high rate capability for all the alkali ions, Li migration in K_xVPO_4F (x~0) is more difficult than Na and K. This work suggests that a large cavity is not always good for insertion of alkali-ions and cathode materials need to be suitably tailored to each intercalating ion species.

1. Introduction

Electrochemical energy storage of renewable energy is of considerable societal interest. . Rechargeable batteries, including Li-ion (LIBs), Na-ion (NIBs), and K-ion batteries (KIBs) have been studied as potential energy storage systems.[1-5] Among these, KIBs are particularly interesting because graphite can intercalate K ions reversibly, making it a possible anode material for KIBs,[6-7] and because the standard redox potential of K/K^+ is lower than that of Na/Na^+ and even Li/Li^+ in non-aqueous electrolytes, translating into a potentially higher working voltage.[6]

Intense efforts have focused on the development of high-voltage cathodes for KIBs. In particular, many polyanionic compounds have been investigated as high-voltage cathodes for KIBs.[8-13] For example, Recham *et al.* reported $KFeSO_4F$ as a cathode for KIBs; this material provides an average voltage of ~3.6 V *vs.* K/K^+ with a reversible capacity of ~100 mAh g^{-1}.[8] K_xVPO_4F and K_xVOPO_4 were evaluated as K-cathodes by Chihara *et al.* and found to discharge ~92 mAh g^{-1} at an average voltage of ~4.1 V *vs.* K/K^+ and ~80 mAh g^{-1} with an average voltage of ~4.0 V *vs.* K/K^+, respectively.[9] We recently demonstrated that the performance of K_xVPO_4F can be improved to ~105 mAh g^{-1} and ~4.33 V *vs.* K/K^+ through the synthesis of more stoichiometric K_xVPO_4F.[10] We also found that partial oxygen substitution in K_xVPO_4F disorders the anion sublattice, which reduces achievable capacity and voltage. [10]

In continuing our efforts to understand the structure–property relationship in electrode materials, we investigate and contrast in this work the alkali-ion (K, Na, and Li) intercalation properties of K_xVPO_4F. We observe that the K_xVPO_4F (x~0) cathode can deliver reversible capacities of ~90–100 mAh

g^{-1} with high average voltages of ~4.3, ~3.98, and ~3.96 V in K, Na, and Li cells, respectively. We attribute the lowest voltage for Li, as compared to Na intercalation, to the large cavity size in the K_xVPO_4F (x~0) framework, which leads to undercoordination for Li ions. The K_xVPO_4F (x~0) cathode exhibits stable cycling and high rate capability in K, Na, and Li cells. However, we find that Li insertion into K_xVPO_4F (x~0) is more difficult than Na and K despite its small ionic radius.

2. Results

2.1. **Material characterization**

Figure 1a presents an XRD pattern and refinement results for K_xVPO_4F. The refinement of the as-prepared K_xVPO_4F with $Pna2_1$ space group yields lattice parameters of a = 12.817(8), b = 6.395(4), and c = 10.600(5), which agree well with previous results in the literature.[10] While the peak positions are well fitted with the $Pna2_1$ based structure, the minor mis-match in peak shape and intensity might point at particle size/strain effects or partial disorder which we did not include in the refinements. Figure 1b presents a SEM image of K_xVPO_4F. To obtain a better SEM image without effects of charging, the K_xVPO_4F particles were mixed with conductive carbon. The primary particle size of $KVPO_4F$ is estimated to be ~100–200 nm. The small particles at the top of Figure 1b are the carbon additive. After the electrode preparation, the particle size and morphology are not changed (Figure S1).

2.2. **Electrochemical cycling of K_xVPO_4F (x~0) in K, Na, and Li cells**

Figure 2a–c present the electrochemical charge and discharge profiles of K_xVPO_4F (x~0) electrodes in K, Na, and Li cells, respectively. Preceding the electrochemical measurements in K, Na and Li cells, the K_xVPO_4F (x~1.0) cathode was fully charged to 5.0 V (*vs.* K/K^+) in a K cell, and the charged K_xVPO_4F (x~1.0) cathode was reassembled in K, Na and Li cells. Once the charge voltage reaches 5.0 V we hold it there for 5 hours to remove all the K ions from the structure. The specific capacity of the first charge is 166 mAh g^{-1} (Figure S2). The specific capacity is calculated based on the weight of the $KVPO_4F$ cathode so that the theoretical capacity is 128 mAh g^{-1} for all three electrodes. The extra capacity in the first charge process can likely be attributed to electrolyte decomposition at high voltage.

To confirm complete K extraction, we characterized K_xVPO_4F with *ex situ* XRD and XPS as shown in Figure S3-4. The XRD pattern of the charged K_xVPO_4F (x~0) is in agreement with the simulated XRD for K_0VPO_4F, suggesting that most K ions are extracted during the charge process. However, the quality of the *ex situ* lab-XRD pattern is not high enough to perform a reliable refinement and determine the remaining K amount in the structure. The *ex situ* XPS analysis shows that the peaks for K at 292.9 and 295.8 eV completely disappear after K extraction, indicating that there is almost no K left in the charged K_xVPO_4F. The peak located at ~291.1 eV is attributable to the formation of solid electrolyte interphases (SEI) that form during the first charge. Upon discharge, the peaks for K reversibly evolve while the SEI peak remains.

In the K cells, the K_xVPO_4F (x~0) cathode delivers capacities of 129 and 93 mAh g^{-1} during the first charge and discharge, respectively, with an

average voltage of ~4.33 V *vs.* K/K^+ (Figure 2a). The K_xVPO_4F (x~0) cathode exhibits a capacity of 122 mAh g^{-1} for the first charge and 106 mAh g^{-1} for the first discharge in Na cells (Figure 2b). An average voltage of ~3.98 V (*vs.* Na/Na^+) is observed in the Na cells. In the Li cells, the K_xVPO_4F (x~0) cathode achieves a capacity of ~119 mAh g^{-1} and ~91 mAh g^{-1} for the first charge and discharge, respectively, and average voltage of ~3.96 V (*vs.* Li/Li^+), as shown in Figure 2c. The charge and discharge voltage profiles of K_xVPO_4F (x~0)are unchanged during the electrochemical cycling in each cell, indicating reversible alkali-ion de/intercalation. This is confirmed by the cycling stability shown in Figure 2d. In K, Na, and Li cells, the K_xVPO_4F (x~0) cathode maintains respectively ~77%, ~77%, and ~79% of the initial discharge capacity after 100 cycles. We contrast the average voltage of the K_xVPO_4F (x~0) cathode in K, Na, and Li cells in Figure 2e, where we plot the average voltage of each cell *vs.* the standard hydrogen electrode (SHE) potential in propylene carbonate solvent.[6] The values in Figure 2e were obtained by adding the SHE potential of M/M^+ (M=Li, Na, and K) in carbonate solution to the average voltage of the cathode (*vs.* M/M^+). To eliminate the effect of polarization, we plot the average of the charge and discharge voltages. Insertion of K, Na, and Li in K_xVPO_4F (x~0) occurs at 1.45, 1.42, and 1.17 V (*vs.* SHE), respectively, indicating that the average voltage of K_xVPO_4F (x~0) decreases with decreasing intercalating ion size from K^+ to Li^+. As the charged state is the same in all the cases (K_xVPO_4F, x~0), the electrochemical voltage is determined by the energetics of the discharged state alone (K_xVPO_4F *vs.* Na_xVPO_4F *vs.* Li_xVPO_4F). We expect that the large

cavities for alkali ions in the K_xVPO_4F (x~0) framework preferentially intercalate K and Na ions, forming more stable compounds and thus leading to a higher voltage than for Li intercalation. Note that for Li and Na other crystal structures are more thermodynamically stable at the discharge composition. High-temperature synthesis of $LiVPO_4F$ forms a tavorite structure [14] while $NaVPO_4F$ forms in a tetragonal or monoclinic structure [15] As an example, we contrast the crystal structure of $KTiOPO_4$-type Li_xVPO_4F and tavorite $LiVPO_4F$ in Figure S5. The discharged Li_xVPO_4F in our work has an orthorhombic crystal structure while the tavorite is triclinic. The coordination and connectivity is different in these two structures: in our Li_xVPO_4F, there are two distinct type of VO_4F_2 octahedra: F atoms occupy equatorial positions around one V and axial positions around the other V, and the VO_4F_2 octahedra form zig-zag chains. In contrast, in tavorite $LiVPO_4F$ the F atoms sit in equatorial positions and the VO_4F_2 octahedra are interconnected forming linear chains.

Ex situ XRD characterization for the charged K_xVPO_4F (x~0) and discharged K_xVPO_4F, Na_xVPO_4F, and Li_xVPO_4F, shown in Figure S6, demonstrates that the charged structure is the same for all K, Na, and Li cells and that the $KTiOPO_4$-type structure is recovered after K, Na, and Li intercalation, indicating a topotactic reaction to a metastable state for Na_xVPO_4F and Li_xVPO_4F. *Ex situ* XPS experiments demonstrate that the alkali ion intercalation is accompanied with $V^{3+/4+}$ redox (Figure S7). To understand in more detail how each ion intercalates, we compare the calculated crystal structures of K_xVPO_4F, Na_xVPO_4F, and Li_xVPO_4F. We find that in the discharged compounds the Li-V distance (3.17 Å) is much

shorter than the Na-V (3.41 Å) and the K-V (3.56 Å) ones. In addition, as presented in Figure S8, the K and Na ions are located in the same sites, K1 and K2, where they are coordinated by six O^{2-} ions and two F^{-} ions. In contrast, the Li ions prefer a site that has planar coordination with two O^{2-} ions and two F^{-} ions (Li1), and a site that has planar coordination with four O^{2-} ions (Li2) (see Figure S9). The unusual coordination of Li (planar coordination) further indicates that the K_xVPO_4F (x~0) host with the $KTiOPO_4$ structure is not a low energy structure for that compound. This is consistent with the fact that $LiVPO_4F$ forms a tavorite structure when synthesized at high temperature. The relative decrease of Li-insertion voltage compared to K-insertion is likely due to the short Li-V distance and the unusual coordination of Li which usually prefers a tetrahedral or octahedral anion geometry (Table S1 and Figure S9). The calculated average voltages are 4.34 V (*vs.* K/K^+) for K intercalation, 3.88 V (*vs.* Na/Na^+) for Na intercalation, and 3.94 V (*vs.* Li/Li^+) for Li intercalation. These values translate to 1.46, 1.32, and 1.15 V *vs.* SHE, respectively, which is consistent with the experimental trend that the average voltage decreases with decreasing intercalating ion size.

2.3. Rate capability

The rate capability of K_xVPO_4F (x~0) in K, Na, and Li cells in discharge was tested by charging at 30 mA g^{-1} and discharging at various current rates ranging from 30 to 2000 mA g^{-1}. The results are shown in **Figure 3a–c**. In K cells, K_xVPO_4F (x~0) cathode delivers 92, 90, 88, 86, 83, 79, 76, 72, and 62 mAh g^{-1} at 30, 50, 100, 200, 500, 800, 1000, and 2000 mA g^{-1}, respectively (Figure 3a). In Na cells, K_xVPO_4F (x~0) cathode provides 99, 98, 94, 90, 87, 83, 80, 77, and 66 mAh g^{-1} at 30, 50, 100, 200, 500, 800,

1000, 2000 mA g^{-1}, respectively, as observed in Figure 3b. Capacities of 90, 89, 85, 81, 78, 75, 72, 66, and 40 mAh g^{-1} are observed for the K_xVPO_4F (x~0) cathode in Li cells at 30, 50, 100, 200, 500, 800, 1000, 2000 mA g^{-1}, respectively (Figure 3c). Figure 3d–e compares the capacity retention of K_xVPO_4F (x~0) with increasing current in K, Na, and Li cells. At a high current of 2000 mA g^{-1} (~15C, where 1C = 128 mA g^{-1}), K_xVPO_4F (x~0) retains 67.5% (K), 67% (Na), and 44.69% (Li) of its low-rate capacity. Interestingly, once the current density is higher than 800 mA g^{-1} (6.25C), worse rate capability is observed for Li intercalation than for Na and K despite its smaller ionic radius These results indicate that the kinetics of Li intercalation in K_xVPO_4F (x~0) is slower than for K and Na, the origin of which we investigate in the next section.

2.4. **K, Na, and Li migration barriers in K_xVPO_4F (x~0) cathode**

Figure 4 shows the *ab-initio* calculated K-ion migration barriers of three possible paths in the K_xVPO_4F structure. Each path starts and ends in an equivalent site so that it can percolate through the extended crystal. In a pristine K_xVPO_4F structure (without vacancies), K ions are located at two distinct sites, namely K1 and K2. The K ion at the K1 site shares two F ions with two VO_4F_2 octahedra, whereas at the K2 site, K shares two F ions with a single VO_4F_2 octahedron.[10] Interestingly, when a vacancy is formed in the K_xVPO_4F structure, the K ion adjacent to the vacancy spontaneously moves to a new site (K3), which is located between the K1 and K2 sites (Figure S10). This ‘spontaneous K3 migration’ participates in K-ion diffusion along path3, as discussed later. As there is spontaneous K ion migration into the new K3 site in both initial and final structures and they

have the equivalent site occupancy in our K-migration calculations, the energy of these structures is the same although the K1 and K2 site energies are different. (Figure 4). For the NEB calculations, a vacancy is created in a supercell with 16 formula units by removing one K ion at either K1 or K2 site in order to enable a K ion to migrate to the vacant site. Figure 4a shows the migration energy for K along path1 which goes between K1 site and through a K2 site, illustrated in Figure 4b. This path (path1) involves two hops. In the first hop (pink trajectory), the K ion at the K1 site hops to a K2 site. In the second hop (blue trajectory), the K ion moves from this K2 to another K1 site. The overall diffusion direction of this path is along the *a*-axis and has a migration barrier of 421 meV. Path 2 is an alternative pathway between two K1 sites through K2, but this time along the *bc* diagonal direction. The energy and visualization is shown in Figure 4c and 4d for half of the path as the second half is symmetric. The very high migration energy along this path (> 1 eV) as compared to path1 is related to the hexagonal voids K-ion has to pass through. At the transition states of path1 and path2 (asterisks in Figure 4a and 4c, respectively), the K ion passes through hexagonal void1 and void2, respectively. The two hexagonal voids are shown in Figure S11. Four VPO_4F_2 octahedra and two PO_4 tetrahedra bound hexagonal void1 while hexagonal void2 is composed of three VPO_4F_2 octahedra and three PO_4 tetrahedra. Because the K ion gets close to a V ion in these voids, they constitute the bottlenecks for the two K-migration paths. For path2, the distance between the hopping K ion and the nearest V ion at the hexagonal void is only 3.12 Å, which is shorter than that for path1 (3.36

Å). This increased electrostatic interaction likely contributes to the higher K migration barrier along path2 than along path1.

Figure 4e and 4f show the K migration barrier and corresponding trajectory of path3. Each K site in Figure 4f is labeled for clarity, namely B and E are K1-type sites, A and D are K2 sites, and C is a K3 site. Path3 consists of two hops, each of which involves concerted migration. The first hop (0% of the path coordinate in Figure 4e) starts with site C (K3) vacant because the adjacent B (K1) and D (K2) sites are occupied. The first hop (pink trajectory) migrates the K ion from site B to A, forming a vacancy at B. At the same time, the K ion at site D spontaneously moves to site C (K3) because the vacancy formed at the adjacent B site has lowered the energy of that site. The second hop (blue trajectory) migrates the K ion at site E to the vacant D site, while the K ion at site C is simultaneously pushed to site B because of the repulsion between the two K ions. This concerted migration enables K ions to move along the *c*-axis with a migration barrier of 195 meV. The reason the path3 has a low migration barrier is that the K ion passes through larger cavities, composed of eight polyhedra (Figure S12), without traversing the hexagonal voids. The shortest K–V distance in the transition state along path3 is 3.74 Å, which is much longer than that along path1 (3.36 Å) or path2 (3.12 Å). Because the migration barrier of path2 is too high for K ions to migrate, diffusion of K is limited to migration along path1 and path3.

Figure 5 investigates the migration of Na in K_xVPO_4F (x~0). Similar to the pristine K_xVPO_4F structure, there are two sites (Na1 and Na2) in Na_xVPO_4F, with the Na1 and Na2 sites corresponding to the K1 and K2 sites,

respectively. However, in the Na_xVPO_4F structure, there is no locally stable K3 site and corresponding concerted migration, but path2 passes through the local K3 environment. We speculate that this is because Na ions are undercoorniated in the K3 site, which is even larger than the K1 and K2 sites. Figure 5a and 5b show the Na migration barrier and corresponding trajectory for path1. For path1, the Na ion at the Na1 site moves to the Na2 site in the first hop (pink trajectory). In the second hop (blue trajectory), the Na ion migrates from the Na2 to the Na1 site through the hexagonal void1 (Figure S11a), which is represented by a black dashed line. The overall migration direction of path1 is along the *a*-axis with a barrier of 222 meV. Along path2, the Na ion migrates the Na1 to Na2 through the hexagonal void2 (Figure S11b), which is represented as a black dashed line in Figure 5d, followed by another hop back to a Na1 position. The overall migration direction of path2 is along the *b*-axis, and the migration barrier is 297 meV. Along these paths, the energy at the Na2 site (50% of the path coordinate) is approximately 200-meV higher than at the Na1 site (0% or 100% of the path coordinate), which is likely attributable to the shorter Na–V distance at the Na2 site (3.18 Å) compared with that at the Na1 site (3.44 Å). Along path1, the Na ion passes through the hexagonal void1 where the shortest Na–V distance is 3.30 Å, which is larger than that at the Na2 site (3.18 Å). Thus, Na migration through the hexagonal void1 does not result in a significant Na migration barrier and most of the barrier is accounted for by the Na1-Na2 site energy difference. Along path2, however, the energy is highest when

the Na ion traverses the hexagonal void2 where Na is only 3.03 Å away from a V ion.

For comparison, **Figure 6** shows the Li-ion migration barriers for three possible migration paths in Li_xVPO_4F.(path1, path2, and path3) The two Li sites in Li_xVPO_4F are different than the K or Na sites: Li ions have planar coordination with $2O2^-$ and $2F^-$ (Li1) shown in Figure S9a or with $4O2^-$ (Li2) (see Figure S9b). The K site coordinated by $7O^{2-}$ ions and $2F^-$ ions is likely too large for Li to occupy. In Li_xVPO_4F, the Li1 site is about 240 meV higher in energy than the Li2 site. There are several reasons for this energy difference. The Li1 site has more V neighbors than the Li2 site. Whereas the Li2 site is coordinated by $4O^{2-}$ which screen the electrostatic repulsion with the surrounding V ions, the Li1 site is coordinated by $2O^{2-}$ and $2F^-$ creating less effective screening of the interaction with V.

Figure 6a-b show the Li migration barrier and trajectory along path1. A Li ion at a Li2 site first moves through a Li1 site (pink trajectory) into another Li2 site (blue trajectory). This trajectory along the *bc* diagonal direction has a migration barrier of 442 meV. Figure 6c-6d and Figure 6e-f show the migration energy and corresponding trajectory of path2 and path3, respectively. Similar to path1, the Li ion moves from Li2 to Li1 (pink trajectory) and then migrates to another Li2 site (blue trajectory) along path2 and path3. The migration barriers of path2 and path3 are 470 and 629 meV, respectively. At the transition state for each path, the hopping Li ion is coordinated by only two anions, whereas it is coordinated by four anions at the Li1 and Li2 sites. The fact that Li^+ has to squeeze through this anion-anion dumbbell where it is highly undercoordinated creates a

high Li migration barrier. Of the three paths, the migration barrier of path1 is the lowest because the shortest Li–V distance (3.35 Å) at the transition state is longer than that for path2 (2.68 Å) or path3 (2.80 Å). For Na and K, a shorter alkali-vanadium distance correlates with a higher alkali ion migration barrier (Figure S13 and Table S2). However, the opposite trend is observed for Li: path2 has lower Li migration barrier than path3 despite the shorter Li-V distance. This result can be related to the anion species encountered along the trajectory. At the transition state, the Li ion is coordinated by $2O^{2-}$ ions along path2 but by $1O^{2-}$ ion and $1F^{-}$ ion along path3. The F^{-} ions has less screening capability than the O^{2-} ion, and as such may create a stronger interaction with the V ion, even though it is slightly farther away. Moreover, the second shortest Li–V distance for path3 (3.51 Å) is shorter than that for path2 (4.40 Å). These factors may contribute to the higher migration barrier for path3. The migration barriers in $LiVPO_4F$ are relatively high compared with those in $KVPO_4F$ and $NaVPO_4F$, which is likely responsible for the inferior rate capability of $LiVPO_4F$ at 2000 mA g^{-1} observed in Figure 3d–e. The alkali migration barrier is not the only factor controlling rate capability, and phase transitions, electronic conductivity, and electrode preparation can all affect the rate capability. By performing the Li, Na and K tests on the same cathode compound and morphology, and using the same electrode preparation, it is reasonable to expect that these other factors are not responsible for the variation between them. Analysis with potentiostatic intermittent titration (PITT) shows that the Li diffusivity is lower than the Na and K one in the low voltage region (Figure S14).

3. Discussion

This work demonstrates that the K_xVPO_4F (x~0) framework can function as a versatile cathode for alkali ions, including K, Na, and Li. In all the K, Na, and Li cells, the K_xVPO_4F (x~0) cathode delivers good cycling stability and a high discharge rate (Figure 2 and Figure 3, respectively). The stable cycle life and high rate capability of the K_xVPO_4F (x~0) cathode likely result from the large cavity size for alkali ions, which can accommodate alkali-ion intercalation and enable fast alkali-ion migration. Our NEB calculations reveal that K_xVPO_4F, Na_xVPO_4F, and Li_xVPO_4F have migration barriers of 195, 222, and 442 meV, respectively. Figure S15 and Figure S16 summary the migration pathways and barriers of $AVPO_4F$ (A=K, Na, and Li). The K and Na migration barriers are even lower than that for the NASICON-type $Na_3V_2(PO_4)_3$ cathode (353 meV),[16] and the Li migration barrier in the K_xVPO_4F (x~0) cathode is comparable to that for tavorite Li_xVPO_4F (418 meV), a high-rate cathode.[17] These results indicate the K_xVPO_4F (x~0) is a framework for fast alkali-ion intercalation. Interestingly, both experiments and NEB calculations show that that the kinetics of Li intercalation in K_xVPO_4F (x~0) is slower than Na and K. The higher Li migration barrier is attributable to the different site occupancy which leads to a different migration path and transition state where it is only coordinated by two anions. Our work illustrates how different alkali ions can have different migration paths in the same host, and demonstrates that large alkali-ion migration channels are not always good for fast ion diffusion, something that has been earlier observed when comparing Na and Li migration in β-alumina.[18] To achieve high-rate capability, one

needs to design electrode materials in which void space and transition states are suitably tailored to each migrating ion species.

In **Figure 7**, we show the average voltage of the VPO_4F cathode in K, Na, and Li cells compared with that of other vanadium-redox-based polyanion cathode materials. The working voltage of K-VPO_4F is the highest for all reported K cathodes[11, 13, 19-23] and higher than $KVPO_{4+x}F_{1-x}$[9-10] and $KVOPO_4$[9]. In the Na cell, K_xVPO_4F (x~0) provides a high voltage of 3.98 V (*vs.* Na), which is the highest ever reported voltage in a vanadium-based polyanion cathode for NIBs, including $Na_3V_2(PO_4)_3$,[24] $Na_3V_2(PO_4)_2F_3$,[25] $NaVPO_4F$,[26] and $NaVOPO_4$.[27] The voltage of 3.96 V (*vs.* Li) in a K_xVPO_4F (x~0)/Li cell is comparable to that of $LiVPO_4F$[28] and $Li_3V_2(PO_4)_3$[29]. Given the higher standard redox potential of Na/Na^+ than Li/Li^+, it is interesting that K_xVPO_4F (x~0) has a higher voltage in the Na cell than in the Li cell.[6] The lower voltage for Li likely originates from the relatively small ionic size of Li^+ compared to Na^+ or K^+, which makes it less stable in the large Na site of the K_xVPO_4F (x~0) framework. This work suggests that the relative size of the intercalating ion species and the cavity plays an important role in determining the voltage of the alkali ion intercalation.

5. Conclusion

This work investigated the alkali-ion (K, Na, and Li) intercalation properties of K_xVPO_4F (x~0). The K_xVPO_4F (x~0) cathode discharges ~90–100 mAh g^{-1} in K, Na, and Li cells, and for K provides the highest voltage (~4.33 V) observed in a poly-anion cathode. The relatively lower Li intercalation voltage is attributable to the large cavity size in the K_xVPO_4F (x~0) framework, which destabilizes the Li site. The K_xVPO_4F (x~0) cathode also

provides stable cycle life and high rate capability in all the K, Na, and Li cells.

6. Experimental Section

Synthesis

K_xVPO_4F (x~1.0) was prepared using a solid-state method. First, VPO_4 was synthesized by reacting $NH_4H_2PO_4$ (11.5 g, 98%, Alfa Aesar), V_2O_5 (9.05 g, >99.6%, Sigma-Aldrich), and carbon black (1.2 g, Super P, Timcal). The precursors were mixed using wet ball-milling in acetone for 12 h and dried overnight at 100 °C. The mixture was pelletized and then sintered at 750 °C for 4 h under continuous Ar flow. Stoichiometric amounts of KF (99.9%, Sigma-Aldrich) and VPO_4 were homogeneously mixed using a planetary ball mill (Retsch PM200) at 300 rpm for 4 h. The mixture was pelletized and sintered at 650 °C for 8 h with continuous Ar flow.

Structure analysis

The structure of each sample was analyzed using X-ray diffraction (XRD; Rigaku Miniflex 600) with Cu Kα radiation, and the structural parameters were determined using the Rietveld method and Highscore Plus software. Scanning electron microscopy (SEM) images were collected on a Zeiss Gemini Ultra-55 Analytical Field Emission SEM in the Molecular Foundry at Lawrence Berkeley National Laboratory. Air-free XPS measurements were performed on a Thermo Scientific K-Alpha XPS System with a monochromatic Al Ka X-ray source in the Molecular Foundry at LBNL. The sample films were transferred into the XPS system using a Thermo Scientific K-Alpha Vacuum Transfer Module to avoid air exposure. The spectra were acquired with passing energy of 50 eV and a dwell time of 50 ms.

Electrochemical measurements

Electrodes were prepared by mixing the active material (70 wt%), Super P carbon black (Timcal, 20 wt%), and polytetrafluoroethylene (PTFE; DuPont, 10 wt%) binder in an Ar-filled glovebox. Test cells were assembled into 2032 coin-cells in a glovebox with a two-electrode configuration using K, Na, and Li metal counter electrodes. A grade GF/F separator (Whatman, USA) and an electrolyte of 0.7 M KPF_6 in ethylene carbonate/diethyl carbonate (EC/DEC; anhydrous, 1:1 volume ratio), 1 M $NaPF_6$ in EC/DEC, or 1 M $LiPF_6$ in EC/DEC were used. The electrochemical tests were performed on a battery testing station (Arbin Instruments) using cathode films with a loading density of ~4.9 mg cm^{-2}.

Computational methods

Density functional theory (DFT) calculations were performed using the projector augmented-wave (PAW) approach,[30] as implemented in the Vienna ab initio simulation package (VASP).[31-33] The Perdew–Burke–Ernzerhof (PBE) exchange-correlation functional[34] was adopted for all the calculations. To compensate for the self-interaction errors of the generalized gradient approximation (GGA), the Hubbard U correction was employed.[35] The U value for vanadium was set to 5.0 eV, as used in a previous study of K_xVPO_4F.[10] A gamma-centered 2 × 3 × 2 k-point grid was used, and the planewave cutoff energy was set to 520 eV. The structures of Na_xVPO_4F and Li_xVPO_4F were constructed by substituting K in K_xVPO_4F with the corresponding alkali elements. Because the alkali-ion sites are partially occupied in the original structural data, all the K-vacancy orderings within a unit cell (8 formula units) were generated, and the 50

configurations with the lowest electrostatic energies were selected using the Pymatgen package.[36] The most stable configurations were then determined from the DFT calculations. The average voltage was calculated using the following equation:[37]

$$V = \frac{-E\left(AVPO_4F\right) - E\left(VPO_4F\right) - E\left(A\right)}{F},$$

where $E(AVPO_4F)$, $E(VPO_4F)$, and $E(A)$ are the calculated energies of $AVPO_4F$, K_xVPO_4F (x~0), and metallic A (K, Na, or Li), respectively, and F is the Faraday constant.

The migration barriers for alkali ions in $AVPO_4F$ were calculated using the climbing image nudged elastic band (CI-NEB) method.[38] For these calculations, 1 × 2 × 1 supercells containing 16 formula units with a gamma-centered 1 × 1 × 2 k-point grid were used. The standard GGA functional was employed as it is difficult to achieve convergence for NEB calculations using GGA + U because of possible metastability of the electronic states along the migration path.[39] In the CI-NEB calculations, only atomic positions were relaxed without changing the lattice parameters and the force is converged within 0.05 eV/Å.

Supporting Information

Supporting Information is available from the Wiley Online Library or from the author.

Acknowledgements

This work was supported by the BIC (Battery Innovative Contest) program of LG Chem, Ltd. under Contract No. 20181787 and Samsung Advanced

Institute of Technology. This work used resources of the National Energy Research Scientific Computing Center (NERSC), a U.S. Department of Energy Office of Science User Facility operated under Contract No. DE-AC02-05CH11231. Work in the Molecular Foundry at LBNL was supported by the Office of Science, Office of Basic Energy Sciences, of the U.S. Department of Energy under Contract No. DE-AC02-05CH11231. H. K. acknowledges the Electrochemical Society for receipt of the Colin Garfield Fink Postdoctoral Summer Fellowship. Y. I. acknowledges support from Japan Public-Private Partnership Student Study Abroad Program.

Received: ((will be filled in by the editorial staff))
Revised: ((will be filled in by the editorial staff))
Published online: ((will be filled in by the editorial staff))

References

[1] V. Etacheri, R. Marom, R. Elazari, G. Salitra, D. Aurbach, *Energy Environ. Sci.* **2011**, 4, 3243.
[2] H. Kim, H. Kim, Z. Ding, M. H. Lee, K. Lim, G. Yoon, K. Kang, *Adv. Energy Mater.* **2016**, 6, 1600943.
[3] H. Kim, J. C. Kim, M. Bianchini, D.-H. Seo, J. Rodriguez-Garcia, G. Ceder, *Adv. Energy Mater.* **2018**, 8, 1702384.
[4] J. C. Pramudita, D. Sehrawat, D. Goonetilleke, N. Sharma, *Adv. Energy Mater.* **2017**, 7, 1602911.
[5] S.-W. Kim, D.-H. Seo, X. Ma, G. Ceder, K. Kang, *Adv. Energy Mater.* **2012**, 2, 710.
[6] S. Komaba, T. Hasegawa, M. Dahbi, K. Kubota, *Electrochem. Commun.* **2015**, 60, 172.
[7] Z. Jian, W. Luo, X. Ji, *J. Am. Chem. Soc.* **2015**, 137, 11566.
[8] N. Recham, G. Rousse, M. T. Sougrati, J.-N. Chotard, C. Frayret, S. Mariyappan, B. C. Melot, J.-C. Jumas, J.-M. Tarascon, *Chem. Mater.* **2012**, 24, 4363.
[9] K. Chihara, A. Katogi, K. Kubota, S. Komaba, *Chem. Commun.* **2017**, 53, 5208.
[10] H. Kim, D.-H. Seo, M. Bianchini, R. J. Clément, H. Kim, J. C. Kim, Y. Tian, T. Shi, W.-S. Yoon, G. Ceder, *Adv. Energy Mater.* **2018**, 8, 1801591.
[11] J. Han, G.-N. Li, F. Liu, M. Wang, Y. Zhang, L. Hu, C. Dai, M. Xu, *Chem. Commun.* **2017**, 53, 1805.

[12] T. Hosaka, T. Shimamura, K. Kubota, S. Komaba, *The Chemical Record* 0.
[13] W. B. Park, S. C. Han, C. Park, S. U. Hong, U. Han, S. P. Singh, Y. H. Jung, D. Ahn, K.-S. Sohn, M. Pyo, *Adv. Energy Mater.* **2018**, 8, 1703099.
[14] B. L. Ellis, T. N. Ramesh, L. J. M. Davis, G. R. Goward, L. F. Nazar, *Chem. Mater.* **2011**, 23, 5138.
[15] J. Zhao, J. He, X. Ding, J. Zhou, Y. o. Ma, S. Wu, R. Huang, *J. Power Sources* **2010**, 195, 6854.
[16] K. M. Bui, V. A. Dinh, S. Okada, T. Ohno, *Phys. Chem. Chem. Phys.* **2015**, 17, 30433.
[17] X. Lv, Z. Xu, J. Li, J. Chen, Q. Liu, *J. Solid State Chem.* **2016**, 239, 228.
[18] M. S. W. a. R. A.Huggins, *NBS Special Publication* **1972**, 139.
[19] J. Liao, Q. Hu, J. Mu, X. He, S. Wang, C. Chen, *Chem. Commun.* **2019**, 55, 659.
[20] H. Kim, D.-H. Seo, A. Urban, J. Lee, D.-H. Kwon, S.-H. Bo, T. Shi, J. K. Papp, B. D. McCloskey, G. Ceder, *Chem. Mater.* **2018**, 30, 6532.
[21] H. Kim, J. C. Kim, S.-H. Bo, T. Shi, D.-H. Kwon, G. Ceder, *Adv. Energy Mater.* **2017**, 7, 1700098.
[22] H. Kim, D.-H. Seo, J. C. Kim, S.-H. Bo, L. Liu, T. Shi, G. Ceder, *Adv. Mater.* **2017**, 29, 1702480.
[23] L. Xue, Y. Li, H. Gao, W. Zhou, X. Lü, W. Kaveevivitchai, A. Manthiram, J. B. Goodenough, *J. Am. Chem. Soc.* **2017**, 139, 2164.
[24] Y. Fang, L. Xiao, X. Ai, Y. Cao, H. Yang, *Adv. Mater.* **2015**, 27, 5895.
[25] M. Bianchini, F. Fauth, N. Brisset, F. Weill, E. Suard, C. Masquelier, L. Croguennec, *Chem. Mater.* **2015**, 27, 3009.
[26] M. Ling, F. Li, H. Yi, X. Li, G. Hou, Q. Zheng, H. Zhang, *J. Mater. Chem. A* **2018**, 6, 24201.
[27] Y. Fang, Q. Liu, L. Xiao, Y. Rong, Y. Liu, Z. Chen, X. Ai, Y. Cao, H. Yang, J. Xie, C. Sun, X. Zhang, B. Aoun, X. Xing, X. Xiao, Y. Ren, *Chem* **2018**, 4, 1167.
[28] M. V. Reddy, G. V. Subba Rao, B. V. R. Chowdari, *J. Power Sources* **2010**, 195, 5768.
[29] Q. Chen, J. Wang, Z. Tang, W. He, H. Shao, J. Zhang, *Electrochim. Acta* **2007**, 52, 5251.
[30] P. Blöchl, *Phys. Rev. B* **1994**, 50, 17953.
[31] G. Kresse, *Phys. Rev. B* **1996**, 54, 11169.
[32] G. Kresse, *Comput. Mater. Sci.* **1996**, 6, 15.
[33] G. Kresse, *Phys. Rev. B* **1999**, 59, 1758.
[34] J. P. Perdew, *Phys. Rev. Lett.* **1996**, 77, 3865.
[35] S. Dudarev, *Phys. Rev. B* **1998**, 57, 1505.
[36] S. P. Ong, W. D. Richards, A. Jain, G. Hautier, M. Kocher, S. Cholia, D. Gunter, V. L. Chevrier, K. A. Persson, G. Ceder, *Compt. Mater. Sci.* **2013**, 68, 314.
[37] M. K. Aydinol, A. F. Kohan, G. Ceder, K. Cho, J. Joannopoulos, *Phys. Rev. B* **1997**, 56, 1354.
[38] G. Henkelman, B. P. Uberuaga, H. Jónsson, *J. Chem. Phys.* **2000**, 113, 9901.

[39] M. Liu, Z. Rong, R. Malik, P. Canepa, A. Jain, G. Ceder, K. A. Persson, *Energy Environ. Sci.* **2015**, 8, 964.

Figures

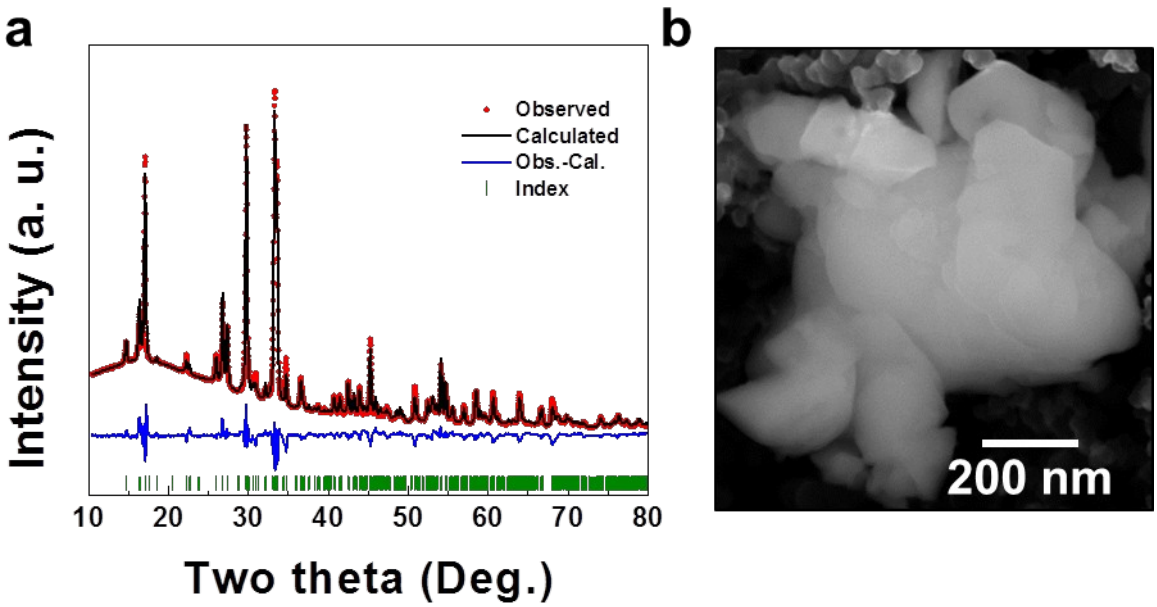

Figure 1. Structure and morphology of K_xVPO_4F. a. Rietveld-refined XRD profile obtained from as-prepared K_xVPO_4F using the $Pna2_1$ space group which provides a good fit (R_{wp} = 5.5). **b.** SEM image of K_xVPO_4F.

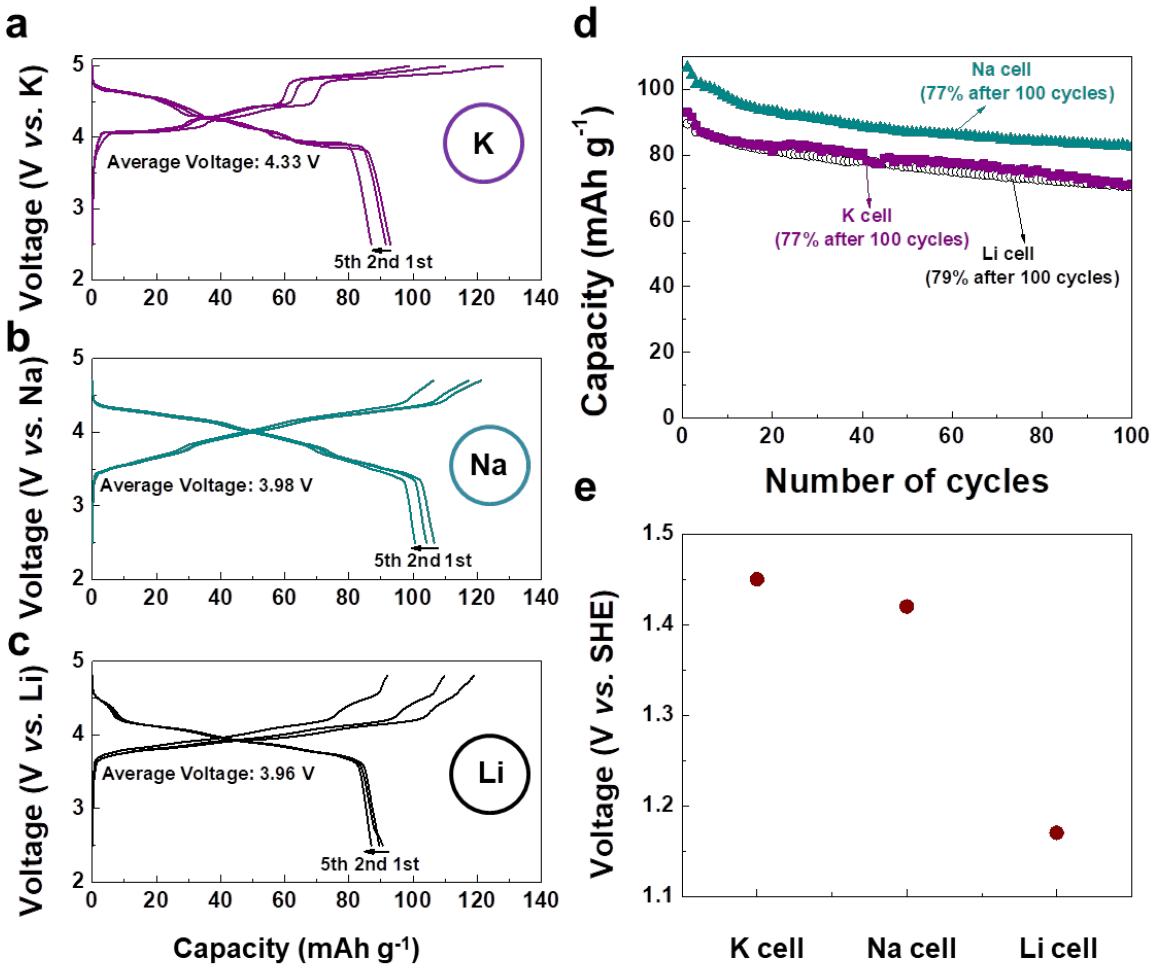

Figure 2. Electrochemical measurements of K_xVPO_4F (x~0) in K, Na, and Li cells. Charge/discharge profiles of K_xVPO_4F (x~0) in **a.** K, **b.** Na, and **c.** Li cells. **d.** Cycling stability of K_xVPO_4F (x~0) in K, Na, and Li cells. **e.** Average voltage of K_xVPO_4F (x~0) *vs.* standard hydrogen electrode (SHE).

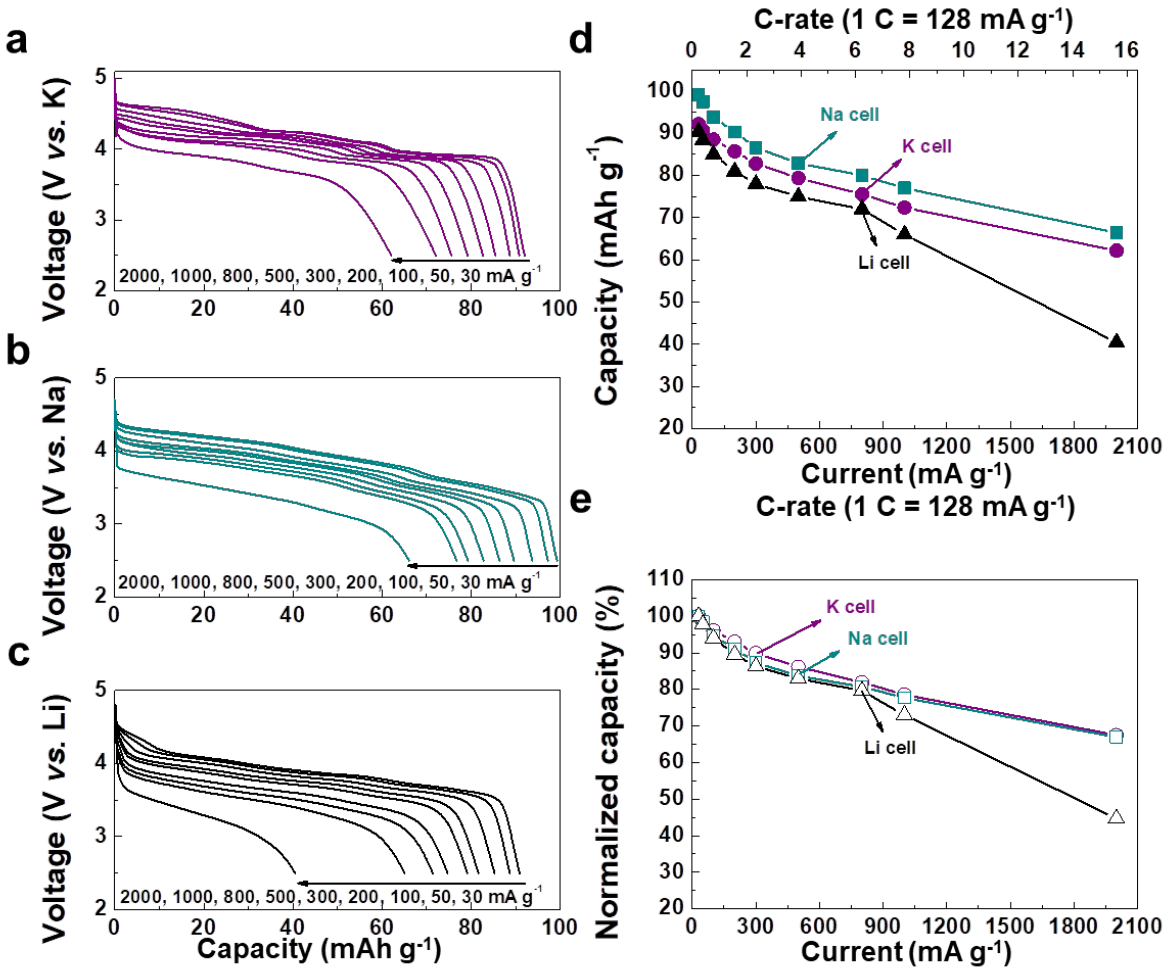

Figure 3. Discharge rate capability of K_xVPO_4F (x~0) in K, Na, and Li cells. Discharge profiles of K_xVPO_4F (x~0) in **a.** K, **b.** Na, and **c.** Li cells at different current rates (30–2,000 mA g^{-1}). **d.** Discharge capacity of K_xVPO_4F (x~0) at different current rates. **e.** Normalized capacity of K_xVPO_4F (x~0) at different current rates.

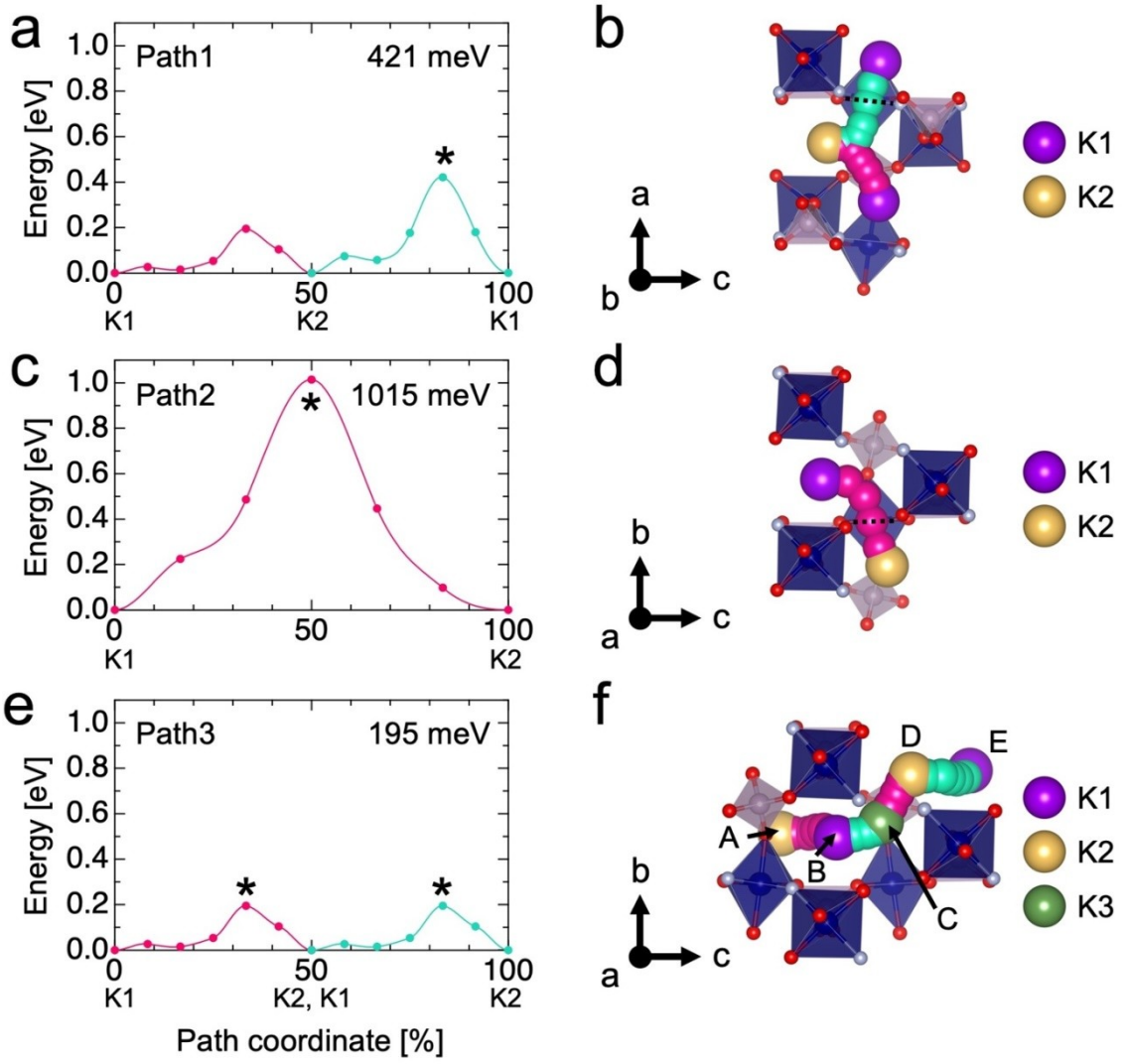

Figure 4. K-ion migration barriers and paths in K_xVPO_4F. a. K-ion migration barrier and **b.** K migration path1; **c.** K-ion migration barrier and **d.** K migration path2; and **e.** K-ion migration barrier and **f.** K migration path3. The asterisks represent transition states. The value of the migration barriers is shown at the top right corner of each plot in a, c, and e. The pink and blue trajectories correspond to the migration barriers of the same color. K1, K2, and K3 denote symmetrically distinct K sites, and the black dashed lines represent cross sections of the hexagonal voids. The K sites along path3 are labeled with A–E for clarity.

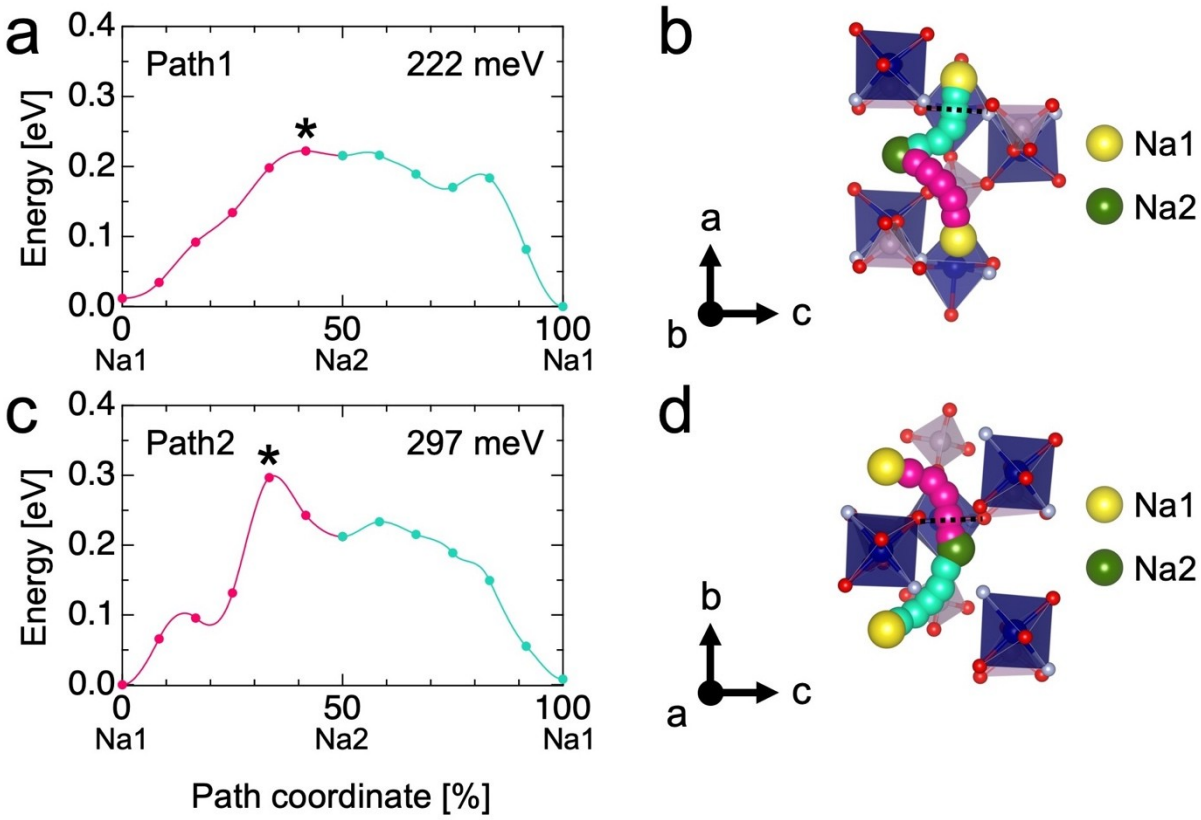

Figure 5. Na-ion migration barriers and migration paths in Na_xVPO_4F. a. Na-ion migration barrier and **b.** Na migration path1; **c.** Na-ion migration barrier and **d.** Na migration path2. The asterisks represent transition states. The value of the migration barriers is shown at the top right corner of each plot in a and c. The pink and blue trajectories correspond to the migration barriers of the same color. Na1 and Na2 denote symmetrically distinct Na sites, and the black dashed lines represent cross sections of the hexagonal voids.

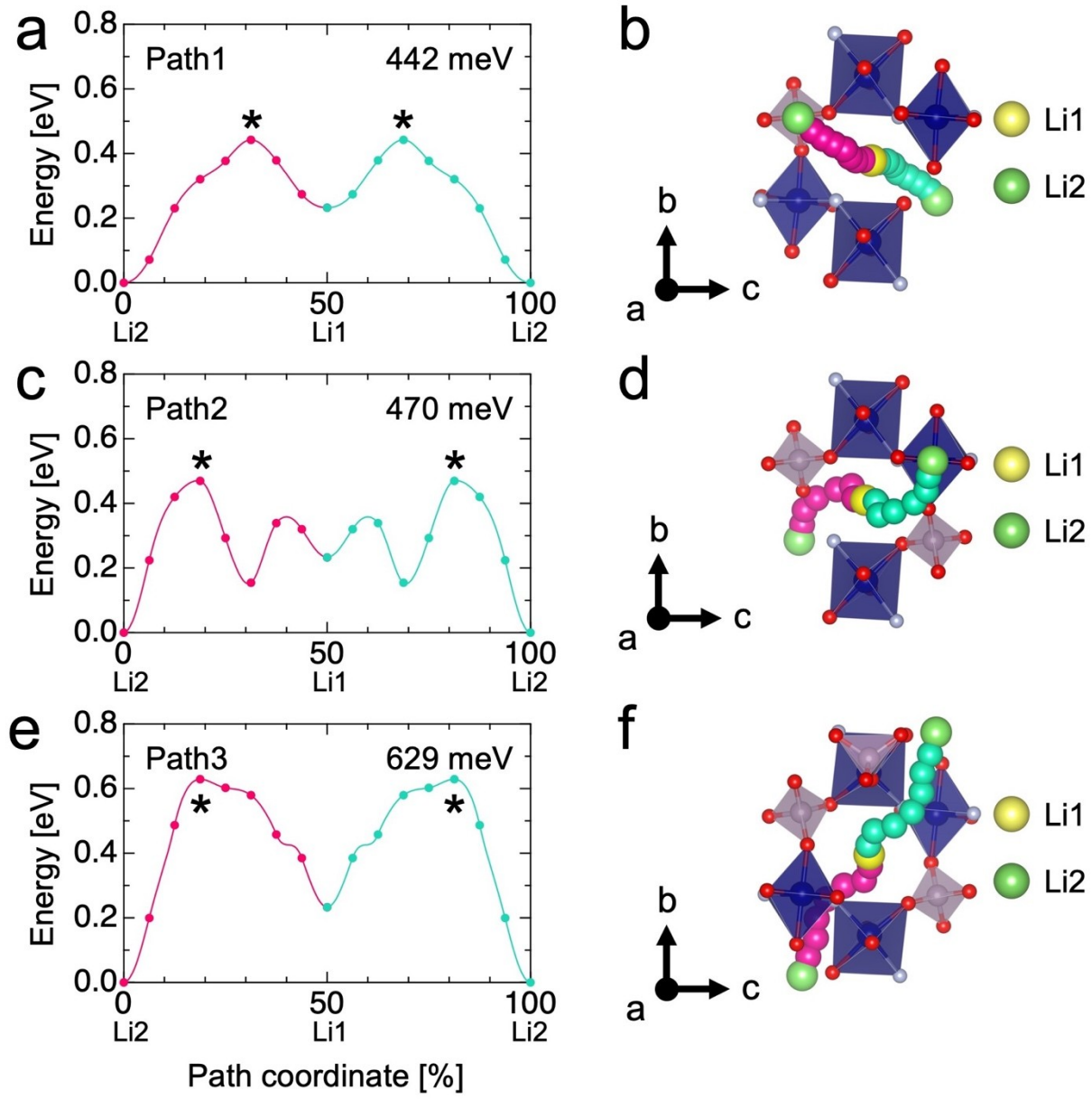

Figure 6. Li-ion migration barriers and migration paths in Li_xVPO_4F. a. Li-ion migration barrier and **b.** Li migration path1; **c.** Li-ion migration barrier and **d.** Li migration path2; and **e.** Li-ion migration barrier and **f.** Li migration path3. The asterisks represent transition states. The value of the migration barriers is shown at the top right corner of each plot in a, c, and e. The pink and blue trajectories correspond to the migration barriers of the same color. Li1 and Li2 denote symmetrically distinct Li sites.

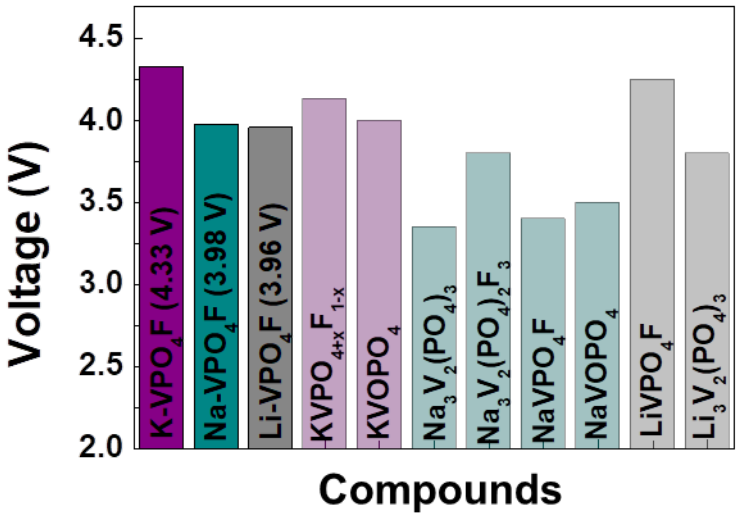

Figure 7. Average voltage of VPO_4F in K, Na, and Li cells and comparison with V-based polyanion cathodes from the literature.[9, 10, 24-29] The number and the height of the bar indicate the average voltage of cathode materials.

Keyword Potassium, Sodium, Lithium, Batteries, Cathodes

Haegyeom Kim, Yuji Ishado, Yaosen Tian, and Gerbrand Ceder*

Investigation of alkali-ion (Li, Na, and K) intercalation in K_xVPO_4F cathode

This work investigates and compares the K, Na, and Li intercalation properties in K_xVPO_4F (x~0) cathode. It demonstrates that large alkali-ion migration channels are not always good for fast ion diffusion and thus cathode materials need to be suitably tailored to each intercalating ion species.

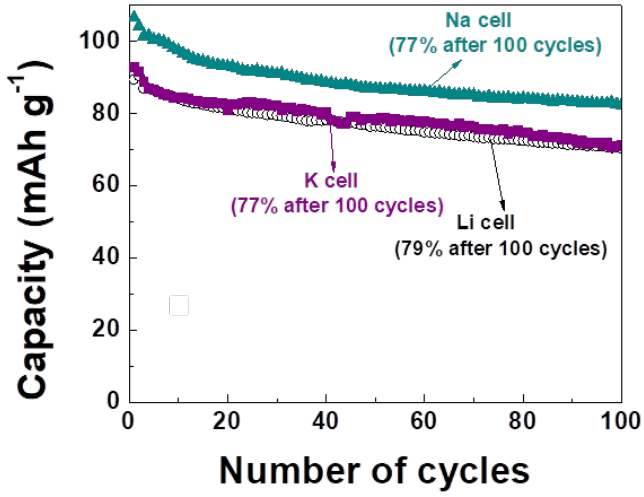

Supporting Information

Investigation of alkali-ion (Li, Na, and K) intercalation in K_xVPO_4F cathode

Haegyeom Kim, Yuji Ishado, Yaosen Tian, and Gerbrand Ceder[*]

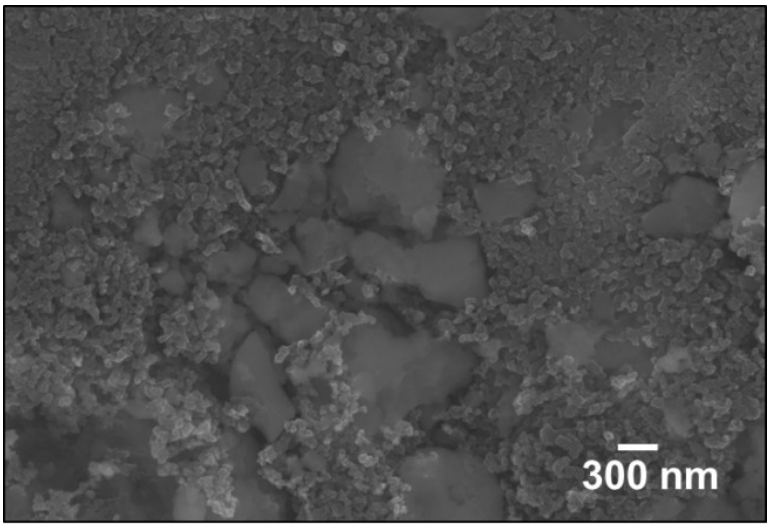

Figure S1. SEM image of as-prepared electrode.

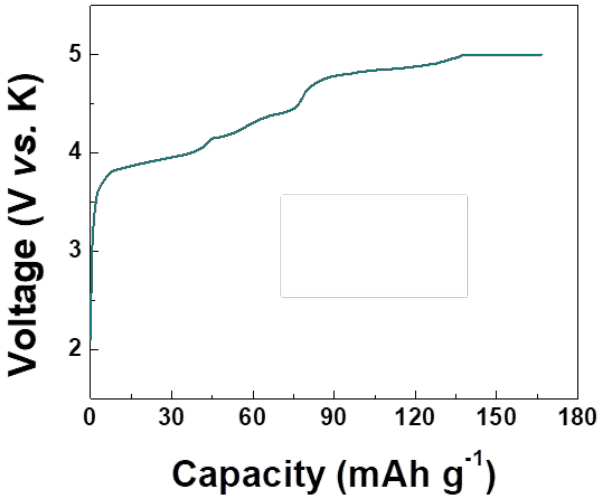

Figure S2. The first charge profile for K_xVPO_4F in a K cell.

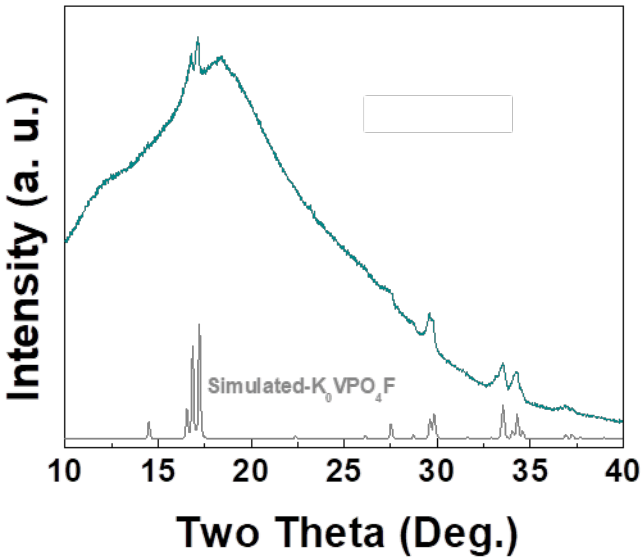

Figure S3. *Ex situ* XRD pattern for charged K_xVPO_4F (x~0).

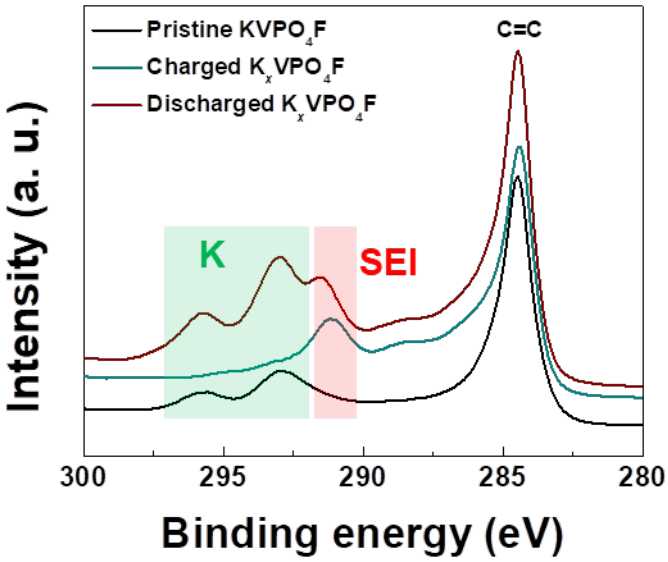

Figure S4. *Ex situ* XPS results of pristine, charged, and discharged K_xVPO_4F.

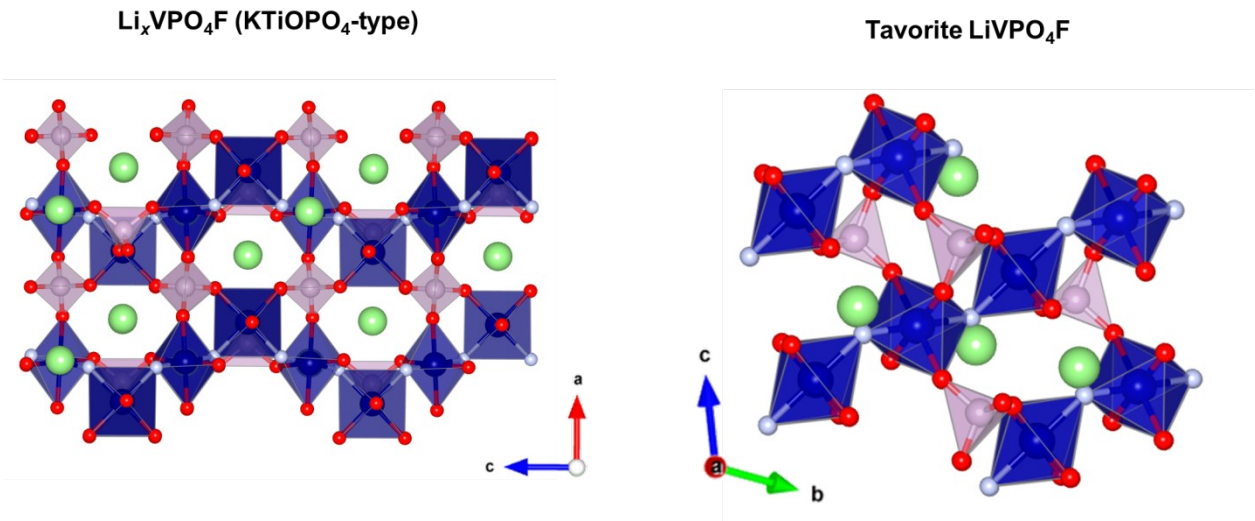

Figure S5. Crystal structure of Li_xVPO_4F ($KTiOPO_4$-type) and Tavorite $LiVPO_4F$.

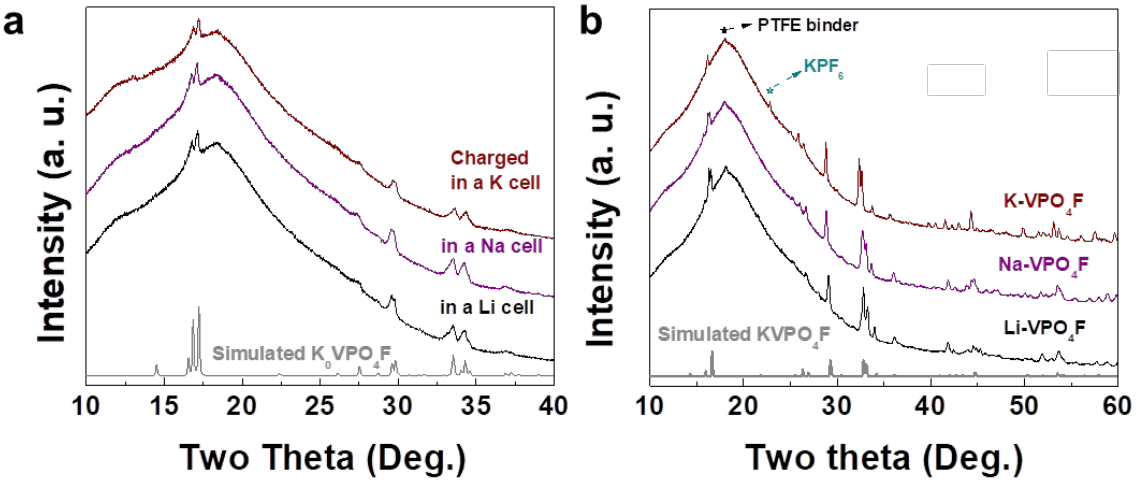

Figure S6. *Ex situ* XRD patterns for **a.** charged K_xVPO_4F (x~0) and **b.** discharged A_xVPO_4F (A=Li, Na, and K) in Li, Na, and K cells.

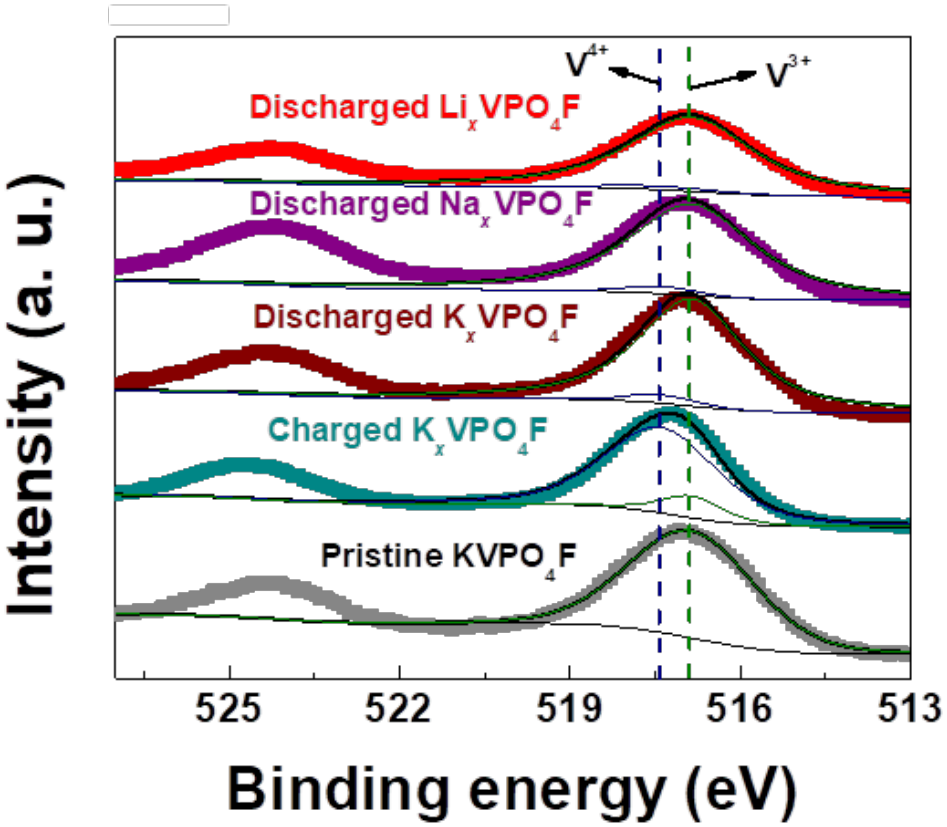

Figure S7. XPS spectra of K_xVPO_4F in charged and discharged states.

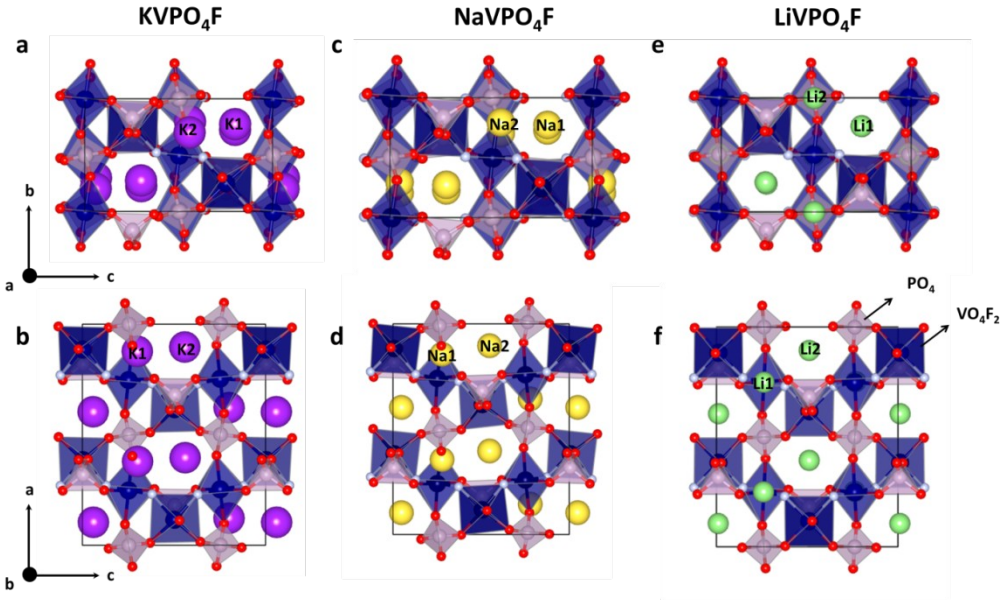

Figure S8. Calculated structures of **a, b** K_xVPO_4F, **c, d** Na_xVPO_4F, and **e, f** Li_xVPO_4F.

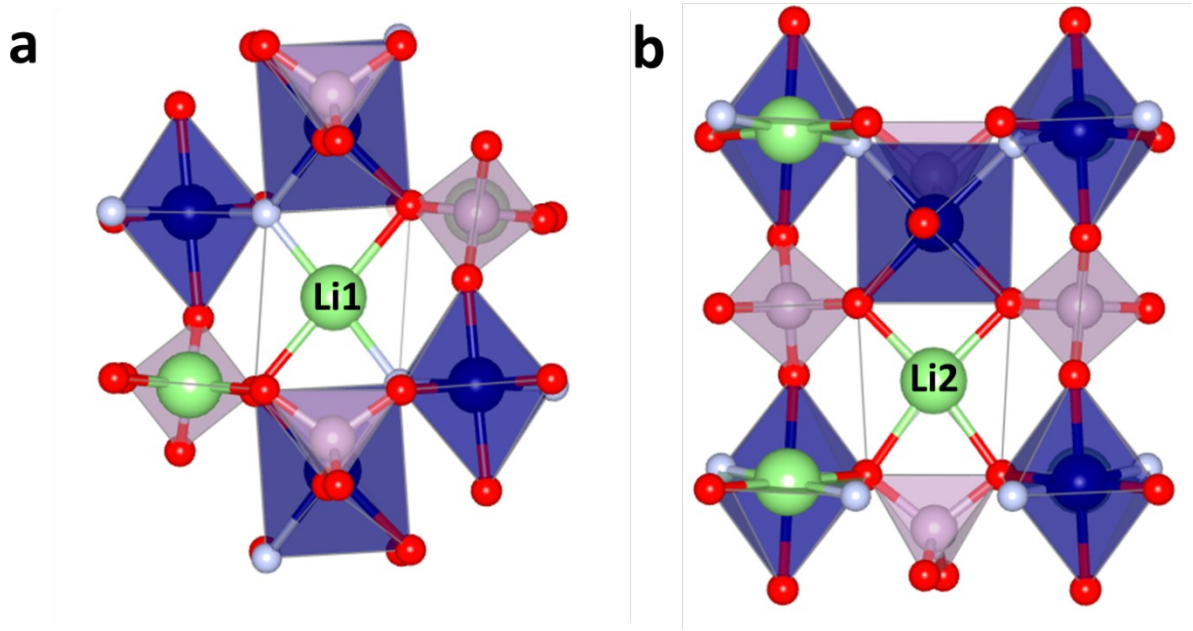

Figure S9. a. Li1 and **b.** Li2 site coordinations in calculated Li_xVPO_4F structure.

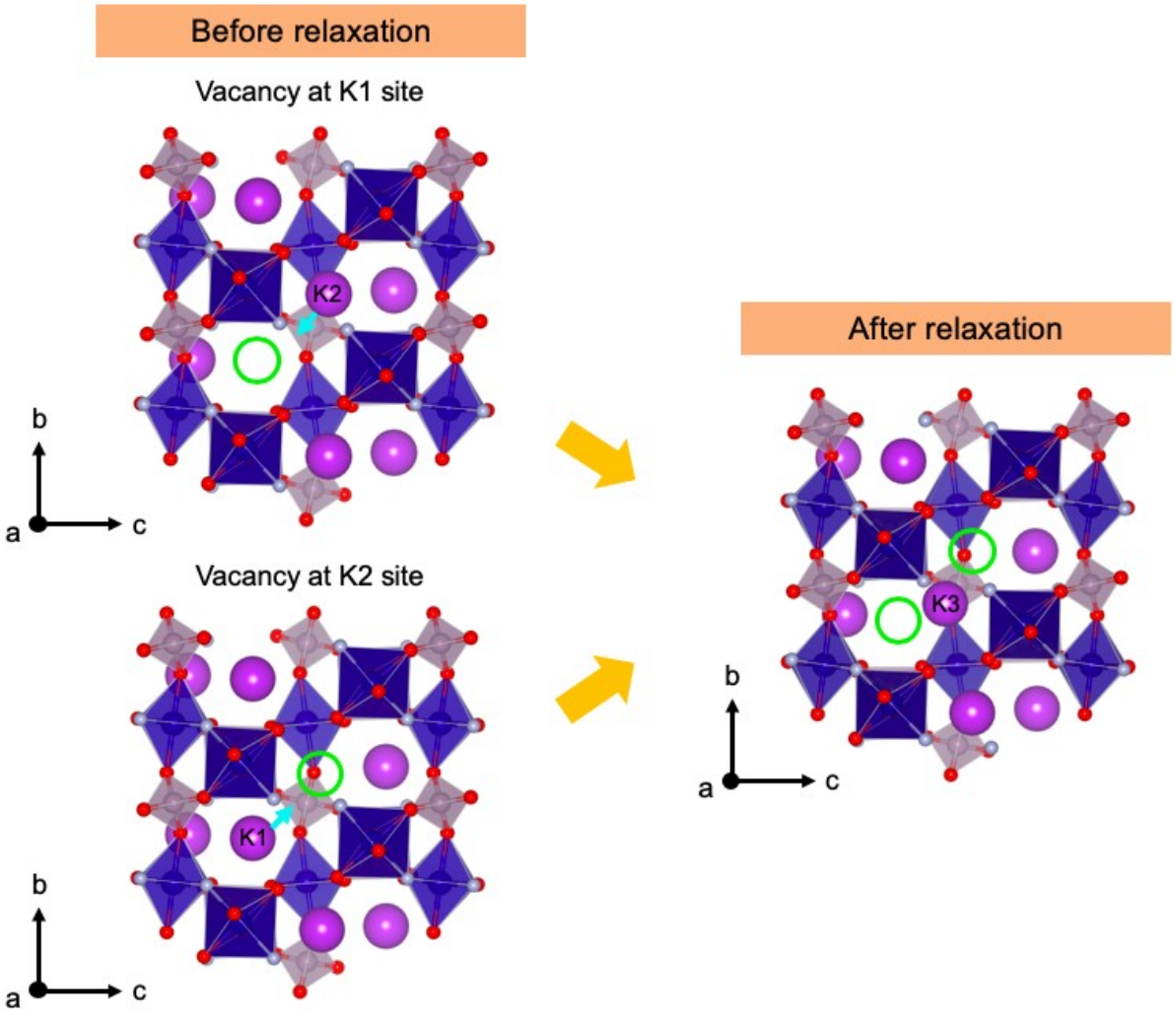

Figure S10. K-ion migration to K3 site during DFT structural relaxation. The K ion adjacent to a vacancy spontaneously moves to a K3 site.

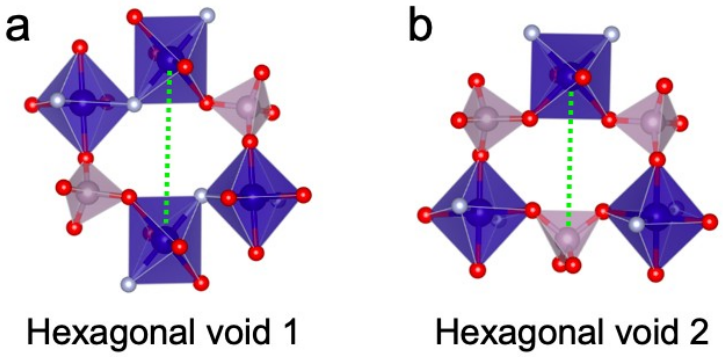

Figure S11. Two types of hexagonal voids in K_xVPO_4F (x~0) framework. **a.** Void1 is composed of four VPO_4F_2 octahedra and two PO_4 tetrahedra. **b.** Void2 is composed of three VPO_4F_2 octahedra and three PO_4 tetrahedra. The dashed lines denote the shortest V–V or V–P distance.

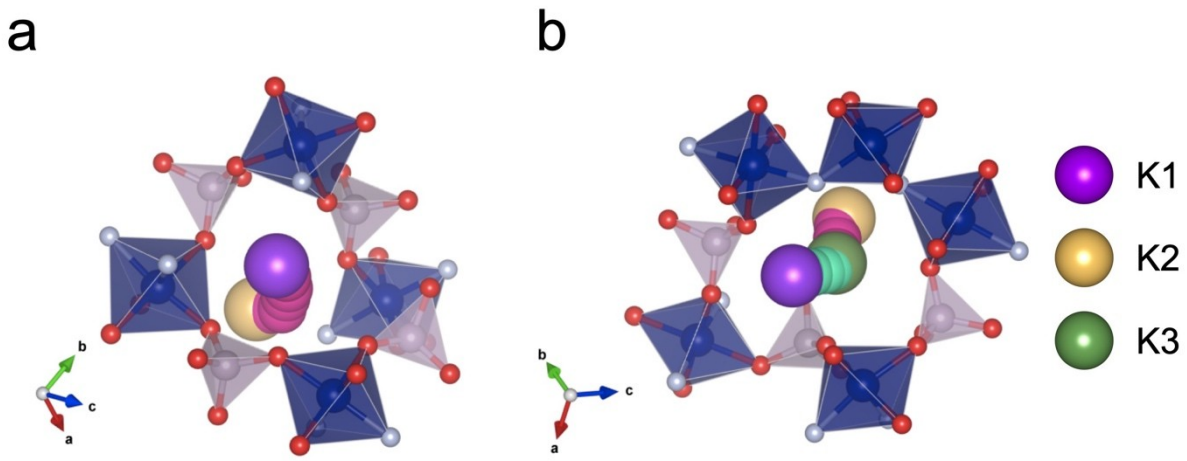

Figure S12. Large voids composed of **a.** four VO_4F_2 octahedra and four PO_4 tetrahedra and **b.** five VO_4F_2 octahedra and three PO_4 tetrahedra. The K ion in K_xVPO_4F passes through these large voids along path3.

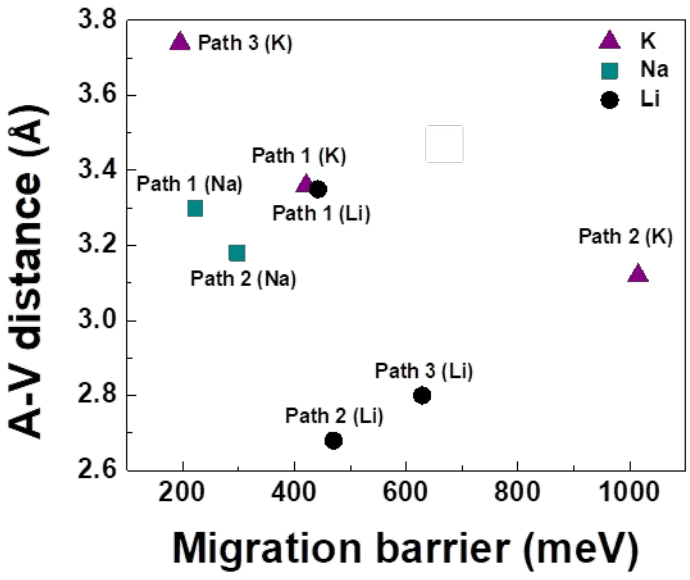

Figure S13. Migration barrier vs. A-V distances (A=Li, Na, and K) in $AVPO_4F$ structure.

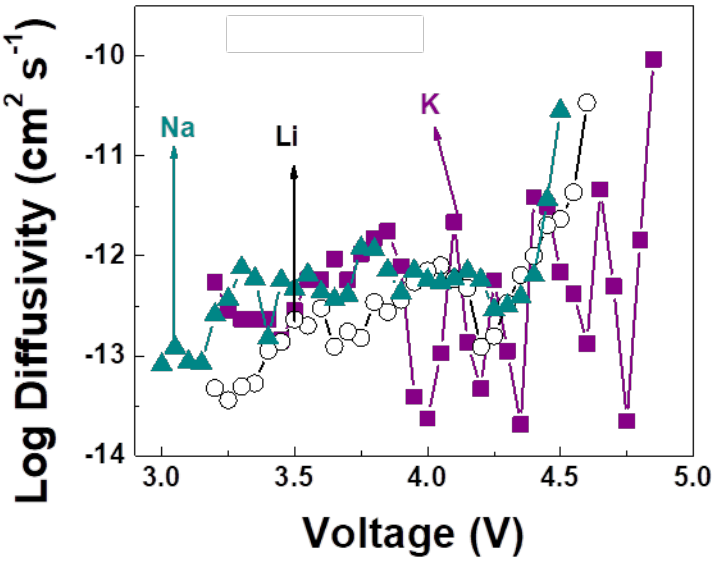

Figure S14. Potentiostatic intermittent titration technique (PITT) to calculate diffusivity of Li, Na, and K in K_xVPO_4F (x~0). PITT was conducted with a voltage step of 5 mV and the current was measured at each constant potential step as a function of time. Each individual titration was complete when the absolute current reached 0.5 mA g^{-1} (C/256 rate). K diffusivity fluctuates more because of more stepped nature of the profile. In part due to thermodynamic factor.[Ref: D. Morgan et al. Electrochem. Sold-State Lett. 2004, 7, A30.]

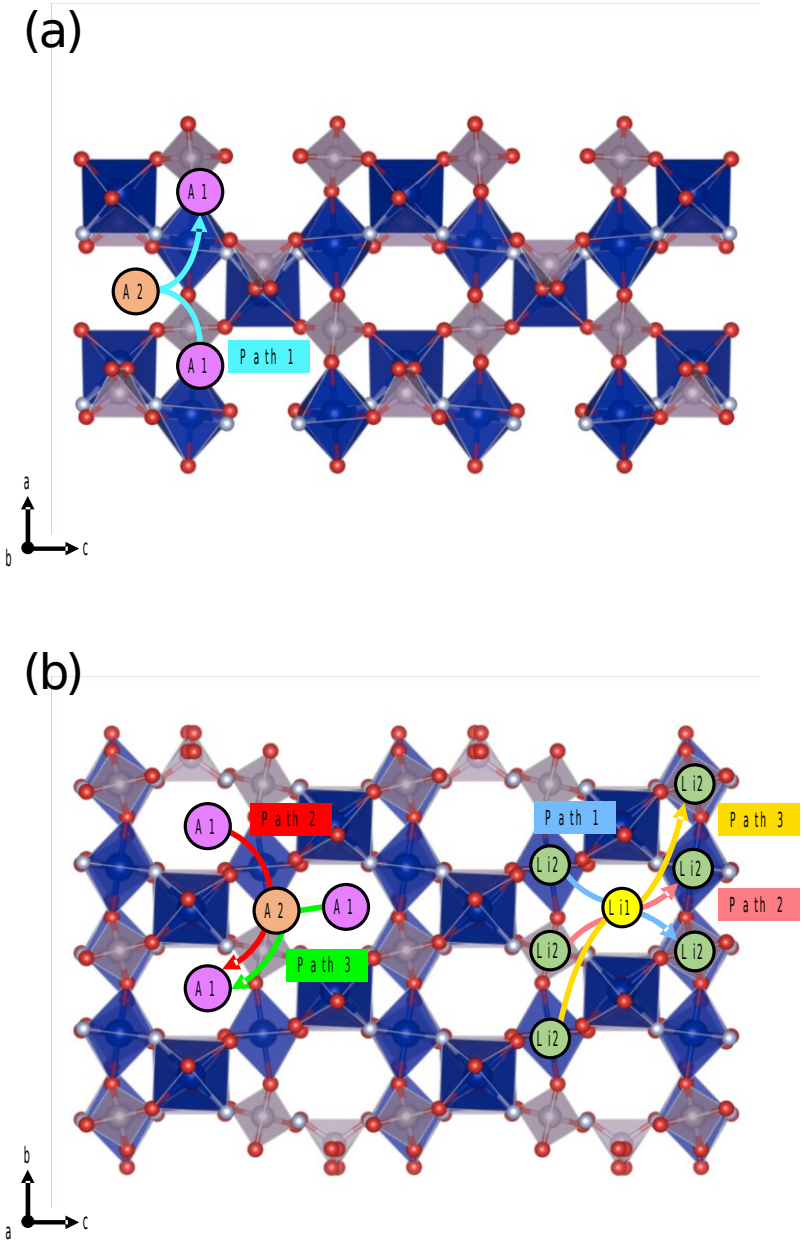

Figure S15. Schematic illustrations of migration pathways. The structures are shown along (a) [010] and (b) [100]. A1 represents K1 and Na1 site, and A2 represents K2 and Na2 site.

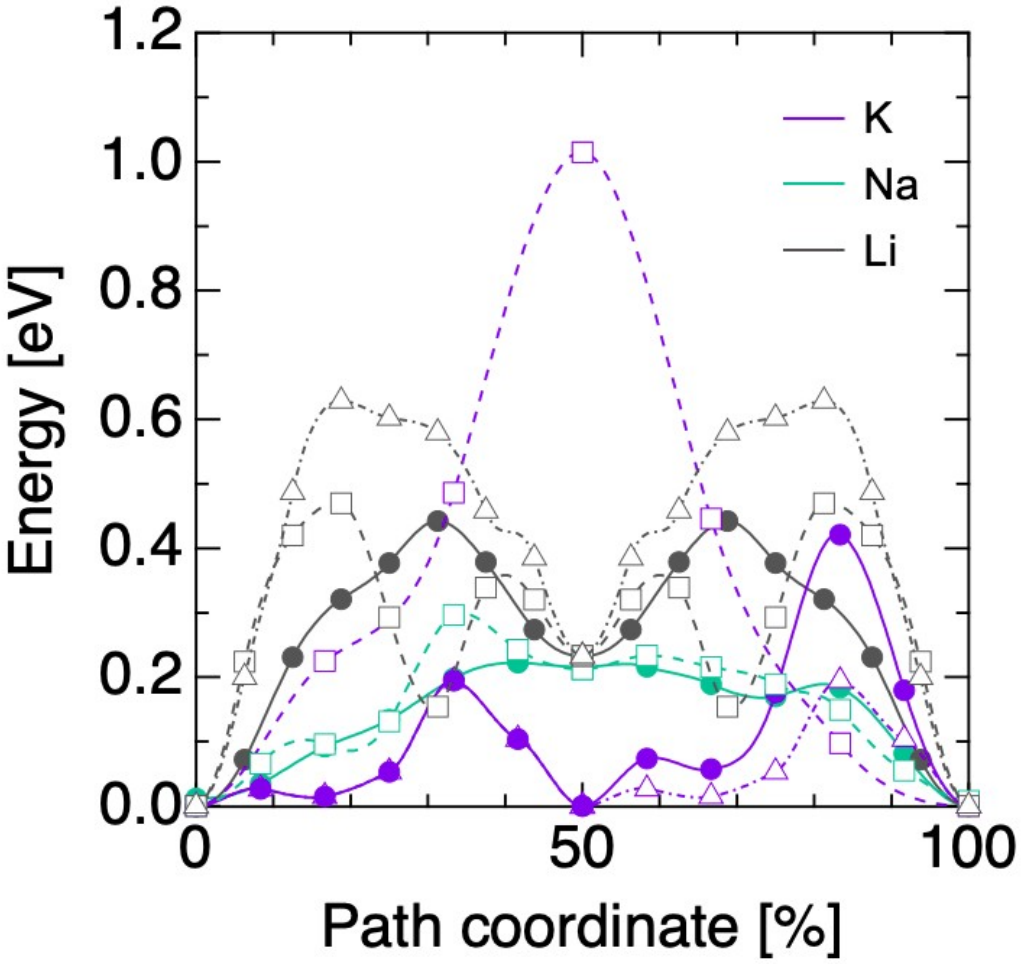

Figure S16. Comparison of migration barriers for K, Na, Li ions. The solid line with the filled circles represents path1, the dashed line with the open squares represents path2, and the dashed dotted line with the open triangles represents path3, respectively.

Table S1. A-V distances and calculated voltage of A_xVPO_4F (A=Li, Na, and K).

A-V distance (A = Li, Na, and K) (Å)	Calculated voltage (V *vs.* SHE)
Li-V: 3.17	1.15
Na-V: 3.41	1.32
K-V: 3.56	1.46

Table S2. A-V distances and alkali ion migration barrier of A_xVPO_4F (A=Li, Na, and K).

A-V distance (A = Li, Na, and K) (Å)	Migration barrier (meV)
Li-V: 3.35	442
Li-V: 2.68	470
Li-V: 2.8	629
Na-V: 3.3	222
Na-V: 3.18	297
K-V: 3.36	421
K-V: 3.12	1015
K-V: 3.74	195